https://doi.org/10.5194/essd-2025-424
Preprint. Discussion started: 18 August 2025

Global biogenic isoprene emissions 2013-2020 inferred from satellite isoprene observations

Hui Li[1,2#], Philippe Ciais[1], Pramod Kumar[1], Didier A. Hauglustaine[1], Frédéric Chevallier[1], Grégoire Broquet[1], Dylan B. Millet[3], Kelley C. Wells[3], Jinghui Lian[1,4], Bo Zheng[2,5]

[1]Laboratoire des Sciences du Climat et de l'Environnement, LSCE/IPSL, CEA-CNRS-UVSQ, Université Paris-Saclay, F-91191 Gif-sur-Yvette, France.

[2]Shenzhen Key Laboratory of Ecological Remediation and Carbon Sequestration, Institute of Environment and Ecology, Tsinghua Shenzhen International Graduate School, Tsinghua University, Shenzhen 518055, China.

[3]University of Minnesota, St. Paul, MN 55108, USA.

[4]Origins.earth, SUEZ Group, Immeuble Altiplano, 4 Place de la Pyramide, 92800 Puteaux, France

[5]State Environmental Protection Key Laboratory of Sources and Control of Air Pollution Complex, Beijing 100084, China.

Correspondence to: Hui Li (hui.li@lsce.ipsl.fr)

Abstract. Isoprene, the most emitted biogenic volatile organic compound, exerts a remarkable influence on atmospheric oxidation capacity, air quality, and climate. Most existing top-down atmospheric estimates of isoprene emissions rely on observational formaldehyde (HCHO) as an indirect proxy, introducing substantial uncertainties due to complex and nonlinear chemical pathways. Recent advances in satellite retrievals of isoprene concentrations from the Cross-track Infrared Sounder (CrIS) enable a direct constraint on isoprene emission inversions. Yet global, multi-year isoprene-based atmospheric inversions are still lacking. Here, we present global, monthly biogenic isoprene emission maps spanning 2013–2020, derived from a mass-balance inversion framework that assimilates CrIS-retrieved isoprene columns into the LMDZ-INCA chemistry–transport model. The global biogenic isoprene emissions average is of 456 ± 200 TgC yr^{-1} over 2013-2020, which is broadly consistent with existing inventories and HCHO-based inversion estimates. The LMDZ-INCA simulations using this estimate of the emissions exhibit improved spatial agreement and reduced biases relative to two independent satellite HCHO retrieval products and to surface observations, confirming the robustness of this inversion framework. The seasonal cycle of emissions is dominated by the Northern Hemisphere, driven by the strong seasonality in temperature and vegetation biomes. Interannually, emissions vary by on average 14 TgC yr^{-1} (1-sigma standard deviation). Two major emission peaks are found in 2015–2016 (456 TgC yr^{-1}) and 2019–2020 (478 TgC yr^{-1}), coinciding with El Niño and widespread extreme heat-wave events, underscoring the dominant influence of temperature anomalies that increase biogenic emissions. Regional analyses identify the Amazon as the largest contributor to the interannual variability, accounting for 22.3% of the global interannual variance in isoprene emissions. Temperature emerges as the primary driver of regional interannual emissions, with its influence modulated by leaf area index, precipitation, and radiation to varying degrees across regions. As one of the earliest attempts at a global, multi-year inversion

https://doi.org/10.5194/essd-2025-424
Preprint. Discussion started: 18 August 2025

based on isoprene observations, this dataset provides input for air quality and climate-chemistry models. The isoprene emission dataset is available at https://doi.org/10.5281/zenodo.16214776 (Hui et al., 2025).

1. Introduction

Isoprene (2-methyl-1,3-butadiene, C_5H_8), the most abundantly emitted biogenic volatile organic compound (BVOC), accounts for 40%-60% of global BVOC emissions, with annual fluxes estimated between 350 and 600 TgC yr^{-1}, showing a considerable uncertainty (Sindelarova et al., 2022; Messina et al., 2016; Wang et al., 2024a). Its emissions are primarily regulated by land cover type, leaf area, climate conditions (e.g., temperature, radiation, precipitation), and atmospheric CO_2 concentration. Among these, land cover, global warming, and rising CO_2 levels drive long-term emission trends, while extreme climate events govern short-term fluctuations. Emission factors (EFs), defined as the rate of emissions per unit area under standardized light and temperature conditions (Henrot et al., 2017), differ substantially among land cover types. Broadleaf trees exhibit the highest EFs, followed by needleleaf trees, grasses, and crops in decreasing order (Opacka et al., 2021; Guenther et al., 2012). Recent studies further indicate that global warming can enhance isoprene emissions from shrubs and sedges, highlighting their emerging role in biogenic fluxes (Wang et al., 2024d; Wang et al., 2024b; Wang et al., 2024c). Of all climate variables, temperature is widely recognized as the primary driver (Seco et al., 2022), yet the variability of its influence across regions is not well characterized. The role of CO_2 is nuanced: although CO_2 fertilization is estimated to have historically enhanced isoprene emissions, future increases in CO_2 concentrations may suppress emissions through physiological inhibition effects (Unger, 2013; Pacifico et al., 2012).

Once emitted, isoprene undergoes rapid atmospheric oxidation, primarily initiated by hydroxyl radicals (OH) (e.g., ~1 h at [OH] = 5×10^6 molecules cm^{-3} at T=298 K) and by ozone (O_3) (Bates and Jacob, 2019). Due to its high reactivity, isoprene plays a pivotal role in tropospheric chemistry: it modulates the oxidative capacity of the atmosphere, influences the atmospheric lifetime of greenhouse gases such as methane (CH_4) (Pound et al., 2023; Zhao et al., 2025), and serves as a major precursor to secondary organic aerosols through condensational growth and new particle formation, which exacerbate regional air pollution (Xu et al., 2021; Curtius et al., 2024). Moreover, isoprene affects O_3 chemistry in a nonlinear manner—acting as a net source under high-NO_x conditions and a net sink in low-NO_x regimes (Geddes et al., 2022). A similar NO_x dependence is observed for formaldehyde (HCHO) yields from isoprene, where elevated NO_x levels accelerate production rates and increase the overall HCHO yield (Wolfe et al., 2016).

Accurately quantifying isoprene emissions is essential for improving air quality forecasts and climate-chemistry model predictions. Two commonly adopted approaches are bottom-up models and top-down atmospheric inversions. Among bottom-up models, the Model of Emissions of Gases and Aerosols from Nature (MEGAN) is the most widely used. It parameterizes isoprene emissions as a function of climate drivers such as light, temperature, and biological variables leaf area index (LAI) and phenology (Guenther et al., 2012). Variability across inventories reflects both differences in parameterizing functional relationships

https://doi.org/10.5194/essd-2025-424
Preprint. Discussion started: 18 August 2025

with climate drivers and, more importantly, inconsistencies in representing vegetation distributions, land-use changes, and EFs (Do et al., 2025; Messina et al., 2016). While improvements are ongoing, bottom-up estimates remain highly uncertain due to these structural limitations and the complex physiological responses of plants to meteorological variability (Cao et al., 2021). Top-down inversion methods offer a complementary strategy by deriving emissions with atmospheric observations. Most existing inversions rely on satellite-retrieved HCHO, a major oxidation product of isoprene, and exploit the spatial correlation between HCHO concentrations and isoprene fluxes (Millet et al., 2008; Barkley et al., 2013; Marais et al., 2012). However, HCHO-based inversions face inherent limitations, including the non-linear nature of isoprene–OH chemistry (Valin et al., 2016), uncertainties in NO_x-dependent HCHO yields, non-zero isoprene/HCHO lifetimes that smear the retrieved isoprene emissions (Wolfe et al., 2016), and contributions from non-isoprene HCHO precursors such as CH_4 and other volatile organic compounds (Nussbaumer et al., 2021).

Direct atmospheric inversion assimilating isoprene concentrations provides a promising alternative to HCHO-based approaches, potentially circumventing those limitations. Historically, this strategy was limited by the lack of atmospheric isoprene observations. Recent advances in infrared remote sensing now enable global retrievals of isoprene concentrations from satellites such as the Cross-track Infrared Sounder (CrIS) (Fu et al., 2019; Palmer et al., 2022; Wells et al., 2022), offering new opportunities for direct inversion. To date, however, isoprene-based inversions remain limited; to our knowledge, only a few studies have been conducted at the regional scale, focusing on areas such as the Amazon Basin, Asia, etc. (Sun et al., 2025; Wells et al., 2020; Choi et al., 2025). No global, multi-year continuous isoprene-based atmospheric inversion has been reported yet.

To fill this gap, we present a global, eight-year (2013–2020), monthly biogenic isoprene emission inversion, based on CrIS-retrieved isoprene concentrations derived through an artificial neural network (ANN) approach (Wells et al., 2020; Wells et al., 2022) and assimilated into the LMDZ-INCA 3D chemistry–transport model. This framework provides a direct top-down constraint on isoprene emissions, overcoming limitations of traditional HCHO-based inversions and enabling the first global, multi-year assessment of isoprene fluxes. The inferred emissions capture key spatiotemporal patterns, including pronounced seasonal cycles dominated by the Northern Hemisphere and two major emission peaks in 2015–2016 and 2019–2020 linked to strong temperature anomalies. These advances highlight the sensitivity of biogenic emissions to temperature variability and demonstrate the potential of CrIS-based inversions to improve emission estimates. The resulting dataset provides a valuable resource for air quality forecasting and climate modeling, and offers valuable insights into biosphere–atmosphere interactions under changing environmental conditions.

2. Methods

2.1 Observations of isoprene and HCHO

This study employs three satellite datasets—CrIS isoprene, TROPOMI HCHO, and OMPS HCHO—along with ground-based HCHO column observations from the Pandonia Global Network (PGN), to derive and

https://doi.org/10.5194/essd-2025-424
Preprint. Discussion started: 18 August 2025

evaluate biogenic isoprene emissions. CrIS, a Fourier transform spectrometer aboard the Suomi National Polar-orbiting Partnership (Suomi-NPP) launched on 28 October 2011, provides daily global observations around 13:30 local time (Han et al., 2013). We use global monthly-mean CrIS isoprene column concentrations from January 2013 to December 2020 (resolution of 0.5° latitude × 0.625° longitude), retrieved using an ANN approach that links spectral indices from CrIS radiances to isoprene columns based on a training dataset constructed from an ensemble of randomized chemical transport model profiles (Wells et al., 2020; Wells et al., 2022). As the ANN retrieval does not include scene-specific vertical sensitivity information, the CrIS-retrieved isoprene columns are directly compared with model-simulated columns. It is noteworthy that CrIS retrievals lack coverage in high-latitude regions north of 60°N (Fig. S1), where the inversion retains their prior emission in this study.

Two independent satellite-based datasets of HCHO column concentrations—OMPS-NM and TROPOMI—are used to indirectly evaluate the posterior-simulated HCHO columns. The instrument OMPS-NM, flown with CrIS on Suomi-NPP, measures backscattered solar radiation in the 300–380 nm range at ~13:30 local time, delivering near-global coverage with a spatial resolution of 50 km × 50 km (Abad, 2022; Nowlan et al., 2023). We use its OMPS_NPP_NMHCHO_L2 retrieval dataset, applying standard quality filters: main_data_quality_flag = 0, solar zenith angle (SZA) < 70°, and cloud fraction < 0.4. TROPOMI, a nadir-viewing hyperspectral spectrometer aboard the European Sentinel-5 Precursor satellite launched in October 2017, provides global HCHO column densities at a similar overpass time (~13:30 local time), with finer spatial resolution (7 km × 3.5 km prior to August 2019 and 5.5 km × 3.5 km thereafter). We use the TROPOMI level 2 product (S5P_L2__HCHO___HiR), filtered by qa_value ≥ 0.75 (ESA, 2020). To ensure comparability with the satellite retrievals in evaluation, modeled HCHO concentrations from LMDZ-INCA are first processed with the averaging kernels (AK) provided with the two satellite HCHO products to generate respective model-equivalent columns, and then resampled to the satellite overpass times (~13:30 local time). All satellite datasets are regridded to a common spatial resolution of 1.27° latitude × 2.5° longitude for consistency. The annual spatial distribution of the three satellite datasets over the globe is shown in Fig. S1.

In addition to satellite data, we also incorporate ground-observed HCHO columns from the PGN network (https://www.pandonia-global-network.org/) for independent evaluation of the posterior simulation of HCHO concentrations. Considering data availability and consistency across all three HCHO datasets, we select the year 2019 as a representative period for the posterior evaluation (Section 3.1).

2.2 LMDZ-INCA global chemistry-transport model

To establish the relationship between isoprene emissions and atmospheric concentrations, we use the LMDZ-INCA global chemistry–aerosol transport model (Hauglustaine et al., 2004). The model is coupled with the ORCHIDEE (Organizing Carbon and Hydrology in Dynamic EcosystEm) land surface model, which dynamically simulates vegetation processes and provides prior estimates of biogenic isoprene emissions using the following formulation (Messina et al., 2016):

https://doi.org/10.5194/essd-2025-424
Preprint. Discussion started: 18 August 2025

$$F = \mathrm{LAI} \times \mathrm{SLW} \times \mathrm{EFs} \times \mathrm{CTL} \times L \quad (1)$$

where LAI is the leaf area index, SLW is the specific leaf weight, EFs denotes the base emissions at the leaf level for a Plant Functional Type (PFT) at standard conditions of temperature (T=303.15 K) and photosynthetically active radiation (PAR=1000 µmol m^{-2} s^{-1}), CTL is the emission activity factor representing environmental responses (e.g., to temperature and light), and L accounts for leaf age-dependent modulation of emissions. A detailed description of the ORCHIDEE-based isoprene emission (global emissions: ~512 TgC yr^{-1}) scheme can be found in Messina et al. (2016).

Global LMDz-INCA simulations are performed at a horizontal resolution of 1.27° latitude × 2.5° longitude, with 79 vertical hybrid sigma-pressure levels extending up to ~80 km, and are nudged to ERA5 wind fields. Monthly global anthropogenic emissions of chemical species and gases are taken from the open-source Community Emissions Data System (CEDS) gridded inventories (Mcduffie et al., 2020), complemented by fire emissions from the Global Fire Emissions Database version 4 (GFED4) (Van Der Werf et al., 2017). For isoprene, monthly mean emissions from the input files are redistributed diurnally based on the local solar zenith angle to account for their strong photochemical dependence. Further details of the LMDZ-INCA configuration are provided by Kumar et al. (2025). A three-year spin-up simulation (2010–2012) is conducted to equilibrate the system, followed by a base simulation for 2013–2020. During the base simulation, isoprene and HCHO concentrations and isoprene emissions are sampled hourly. These hourly outputs are then used for model–observation comparisons and for performing the global inversion of isoprene emissions over the 2013–2020 period.

2.3 Inversion methodology

In order to assimilate CrIS isoprene retrievals into the LMDZ-INCA model, we apply the finite-difference mass balance (FDMB) inversion framework (Cooper et al., 2017). Given isoprene's short atmospheric lifetime, typically a few hours (~3 h at [OH] = 1 × 10^6 molecules cm^{-3} at T=298 K) (Bates and Jacob, 2019; Fu et al., 2019), its horizontal transport is generally limited to a few tens of kilometers, supporting the assumption of a local relationship between emissions and column concentrations. Although this assumption may break down at high latitudes near the poles, its impact is negligible as isoprene emissions are largely confined to 60°S–60°N. In addition, in tropical regions with low NO_2, isoprene-driven OH suppression can prolong its lifetime and potentially violate the local linearity assumption (Wells et al., 2020). A detailed discussion of NO_2 effects is provided in Section 2.4. The final biogenic emissions for each model grid cell and month are calculated as follows:

$$E_{posterior,i,m} = E_{prior,i,m}\left(1 + \beta_{i,m}\frac{\Omega_{obs,i,m} - \Omega_{simu,i,m}}{\Omega_{simu,i,m}}\right) \quad (2)$$

In Eq. (2), i denotes the model grid cell in the 1.27° × 2.5° mesh, m indicates the month, and $\Omega_{obs,i,m}$ and $\Omega_{simu,i,m}$ represent the observed and simulated monthly mean isoprene column concentrations (molecules cm^{-2}), respectively. To account for the strong diurnal variability of the isoprene column, $\Omega_{simu,i,m}$ only considers

https://doi.org/10.5194/essd-2025-424
Preprint. Discussion started: 18 August 2025

the CrIS overpass time (~13:30 local time) in its average, for consistency with $\Omega_{obs,i,m}$. $E_{posterior,i,m}$ and $E_{prior,i,m}$ refer to the posterior and prior isoprene emissions (kgC m^{-2} s^{-1}), respectively. $\beta_{i,m}$ is a dimensionless factor representing the local relative response of modeled isoprene columns ($\Delta\Omega_{simu}/\Omega_{simu}$) to relative changes in prior emissions ($\Delta E_{prior}/E_{prior}$) as calculated below:

$$\beta_{i,m} = \frac{\Delta E_{prior,i,m} / E_{prior,i,m}}{\Delta\Omega_{simu,i,m} / \Omega_{simu,i,m}} \tag{3}$$

To derive $\beta_{i,m}$, we conduct two LMDZ-INCA simulations each year: one using the original ORCHIDEE-based prior isoprene emissions, and the other with those emissions uniformly reduced by 40% (based on the difference between simulated and observational isoprene columns). Sensitivity tests using alternative perturbations (+25%) confirm that $\beta_{i,m}$ is overall insensitive to the choice of perturbation magnitude, with global mean differences around -10% (average ($\beta_{+25\%}/\beta_{-40\%}$) ratio=0.9; Fig. S2). The robustness of β is further discussed in Section 2.4. To avoid extreme changes, we keep $\beta_{i,m}$ within the range 0-10, and the inversion is performed only over land grid cells. An illustration of the spatial distribution of monthly mean β values for 2019 is shown in Fig. S3, with a global annual mean of approximately 0.85. Posterior updates are only applied to grid cells with valid β and CrIS observations, while emissions in the remaining grids are retained at their prior values. During 2013–2020, an average of 67.6% of land grid cells are updated per month, representing 99.0% of prior monthly emissions (Fig. S4), since missing data are concentrated in high-latitude regions with low emissions. For a clearer regional analysis, we divide the globe into 15 regions, as listed in Table 1 and shown in Fig. S5.

Table 1. Regional classification in this study, with classified map presented in Fig. S5.

Abbreviations	Full names
AMZ	Amazon
RSAM	Rest of Southern America (other than Amazon)
EQAF	Equatorial Africa
NAF	Northern Africa
SEAS	Southeast Asia
CHN+KAJ	China+Korea+Japan
SAS	South Asia
SAF	Southern Africa
USA	The United States
MIDE	Mideast
OCE	Oceania
RUS+CAS	Russia+Central Asia
CAM	Central America
EU	Europe
CAN	Canada

2.4 The impact of NO_2 concentration on β

https://doi.org/10.5194/essd-2025-424
Preprint. Discussion started: 18 August 2025

A central assumption in the FDMB inversion framework is the linear response of isoprene concentrations to changes in emissions. However, this linearity is strongly modulated by ambient NO_2 levels and by isoprene itself because both species directly influence the oxidative capacity of the atmosphere and, consequently, the chemical lifetime of isoprene (Wennberg et al., 2018). Under high-NO_2 conditions, isoprene oxidation proceeds efficiently due to rapid OH radical recycling, supporting a robust linear relationship between concentrations and emissions. In contrast, in low-NO_2 environments, the reduced atmospheric oxidizing capacity prolongs the chemical lifetime of isoprene, leading to a superlinear response where concentrations increase disproportionately with emissions (Fu et al., 2019; Wells et al., 2020). This nonlinearity reduces the validity of the linear assumption in regions with low NO_2, necessitating a careful evaluation of β non-linearity and sensitivity to ambient NO_2 levels.

In the LMDZ-INCA simulations, NO_2 emissions are prescribed from the CEDS global inventories (Mcduffie et al., 2020), which cover eleven anthropogenic sectors, including agriculture, energy production, transportation (on-road and non-road), residential, commercial, and international shipping, as well as soil NO_2 emissions from synthetic and manure fertilizers. Detailed configurations are provided in Kumar et al. (2025). Compared to TROPOMI-retrieved NO_2 tropospheric columns from the TROPOMI-RPRO-v2.4 product, LMDZ-INCA simulates an overall negative bias, with NO_2 concentrations approximately 30% lower than observed (Figs. S6–S7). This underestimation of NO_2 leads to an overestimation of isoprene lifetime and, consequently, a systematic underestimation of β in Eq. (3). The effect is particularly pronounced in regions with high isoprene concentrations, consistent with the ~10% reduction of β observed in the +25% isoprene emission perturbation test (Fig. S2).

To assess the robustness of the linearity assumption, we identified grids where the β difference between the +25% and –40% perturbations is within ±20% (i.e., $\beta_{+25\%}/\beta_{-40\%}$ ratio between 0.8 and 1.2 in Fig. S2). These grids account for 70.8% of global isoprene emissions, indicating that the linearity assumption holds across most emissions in this study. It is important to note, however, that the perturbation range (–40% to +25%) represents a substantial 65% change in emissions, which may amplify deviations from linearity. In fact, emission variations are typically smaller; in this study, the posterior emissions are 10.9% lower than the prior, indicating that real-world differences in β are likely modest. As a result, the proportion of emissions for which the linearity assumption remains valid is expected to be even higher.

3. Results

3.1 Evaluation of the posterior simulation of HCHO and isoprene

As shown in Fig. 1, the posterior simulation improves over prior results, both in terms of spatial distribution and correlation with observations. For HCHO, model grid-level comparison against TROPOMI retrievals shows that the global Root Mean Squared Error (RMSE) decreases from 0.29×10^{16} to 0.18×10^{16} molecules cm^{-2}, reflecting a substantial improvement compared to the prior overestimation. Similar improvements are seen when compared with OMPS HCHO retrievals (Fig. S8), indirectly supporting the reliability of the

https://doi.org/10.5194/essd-2025-424
Preprint. Discussion started: 18 August 2025

Open Access Earth System Science Data Discussions

posterior emissions. This enhancement is particularly pronounced over the Amazon, where the RMSE decreases by 0.31 × 10^{16} molecules cm^{-2} (Fig. S9). For isoprene, the model–observation agreement improves more substantially, validating the linearization of LMDZ-INCA based on a perturbation and the assumed local relationship between emissions and column concentrations. The regression slope between posterior simulations and CrIS observations decreases from 2.61 to 1.07, while RMSE reduces from 5.69 × 10^{15} to 1.22 × 10^{15} molecules cm^{-2}. Biases in key tropical regions such as the Amazon are notably reduced, with regional RMSE of isoprene decreasing by 19.59 × 10^{15} molecules cm^{-2} (Fig. S9). In addition to satellite comparisons, posterior-simulated HCHO also shows a modest improvement in agreement with ground-based HCHO column concentrations from the PGN network, with the RMSE decreasing from 0.45 × 10^{16} to 0.42 × 10^{16} molecules cm^{-2} (Fig. S10). These improvements relative to various HCHO observations consistently demonstrate the ability of the inversion framework to derive reliable estimates of the isoprene emissions and enhance model performance across diverse observational benchmarks.

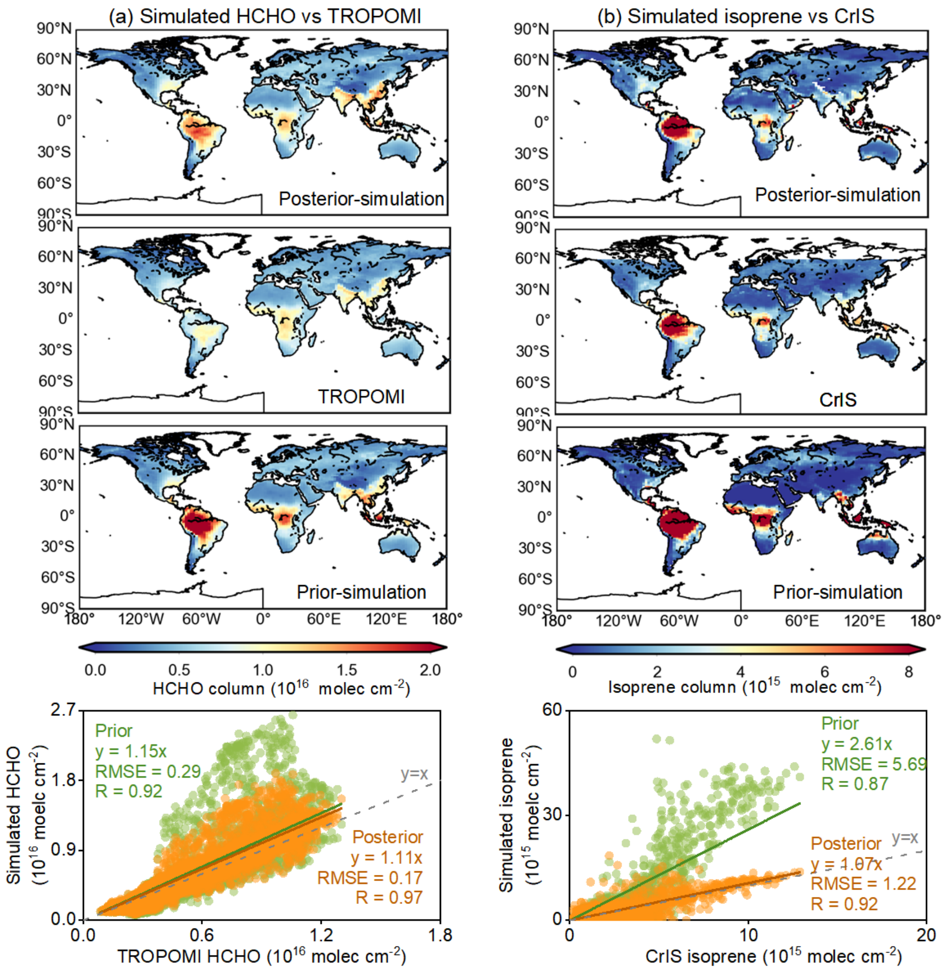

https://doi.org/10.5194/essd-2025-424
Preprint. Discussion started: 18 August 2025

Figure 1. Evaluation of the posterior LMDZ-INCA simulation using TROPOMI HCHO and CrIS isoprene observations in 2019. (a) and (b) present the comparison of the simulated HCHO with TROPOMI observations, and of the simulated isoprene with CrIS observations, respectively. From top to bottom: the global distribution of model grid-scale annual mean of the posterior simulation, satellite observation (from TROPOMI in (a) column and from CrIS in (b) column), prior simulation of the column concentrations, and correlation between annual-mean simulation and observation across the model grid-cells covered by the observation.

3.2 Uncertainty estimation

In the FDMB inversion framework, posterior uncertainty (σ_p) is analytically estimated by minimizing the mass balance cost function, following the formulation of Cooper et al. (2017). It is important to note, however, that σ_p does not account for potential structural errors in the LMDZ-INCA model, such as uncertainties in chemical mechanisms or meteorological fields. This limitation highlights the importance of independently evaluating the posterior estimates against external datasets to assess the robustness and reliability of the inferred emissions (seen in Section 3.1).

$$\frac{1}{\sigma_p} = \frac{1}{\sigma_a^2} + \frac{1}{\sigma_\varepsilon^2} \tag{4}$$

where σ_a and σ_ε represent the relative uncertainties in prior emissions and in the gridded monthly satellite observations, respectively. The prior emissions used in this study are derived from ORCHIDEE, a bottom-up, process-based model. Its uncertainties stem from factors including LAI, SLW, EFs, CTL, and L (as shown in Eq. 1). PFT-dependent EFs vary substantially across different emission inventories, assigned a high uncertainty of 100% (Do et al., 2025; Weber et al., 2023). Among the remaining factors, LAI and the light-dependent fraction (LDF) that controls the CTL term are especially influential. According to Messina et al. (2016), the relative difference in LAI between the ORCHIDEE model and MODIS observations is approximately 50%. Therefore, we assign a 50% uncertainty to LAI, while a 20% uncertainty is applied to the remaining parameters. Applying standard error propagation for multiplicative variables yields a combined prior uncertainty (σ_a) of 117.0%, which represents a rough estimation of the overall uncertainty:

$$\sigma_a = \sqrt{\sigma_{\mathrm{LAI}}^2 + \sigma_{\mathrm{SLW}}^2 + \sigma_{\mathrm{EFs}}^2 + \sigma_{\mathrm{LDF}}^2 + \sigma_L^2} \tag{5}$$

The CrIS isoprene retrievals used in this study are based on an ANN retrieval approach. Retrieval uncertainties are spatially variable, depending on the column concentrations. According to Wells et al. (2022), retrieval uncertainties are generally <25% over high-concentration area ($\geq 10\times10^{15}$ molec cm^{-2}), and >50% in low-concentration area ($<2\times10^{15}$ molec cm^{-2}). To account for this, we apply a piecewise uncertainty function for σ_ε based on the observed isoprene column in each grid cell. An additional 20% uncertainty is applied to account for potential systematic effects, informed by the discrepancies observed in independent dataset comparisons (Wells et al., 2022). Here we assume these two uncertainty components (random retrieval error and systematic error) to be independent and additive in a simplified linear formulation, such that the final observational uncertainty is set at 45% for grid cells with $\Omega_{\mathrm{obs}} \geq 10\times10^{15}$ molec cm^{-2}, 70% for $\Omega_{\mathrm{obs}} < 2\times10^{15}$ molec cm^{-2}, and with linear interpolation in between. Grid cells without valid observations remain at their prior values, and their posterior uncertainties are therefore set equal to the prior uncertainties. Prior and

https://doi.org/10.5194/essd-2025-424
Preprint. Discussion started: 18 August 2025

observational uncertainties are then combined using Eq. (4), and the resulting cell-level posterior relative uncertainties are aggregated to the global scale through area-weighted averaging. Taking 2020 as an example, the spatial distribution of cell-level posterior uncertainties is shown in Fig. 2, with the uncertainty for global annual isoprene emissions estimated at 43.8%.

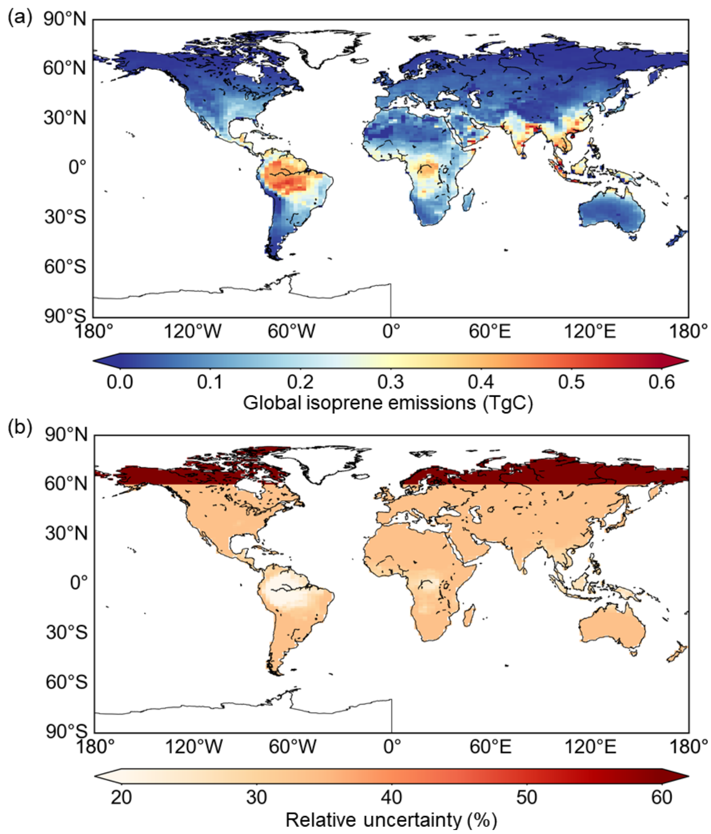

Figure 2. (a) Global distribution of isoprene emissions (TgC per grid cell of 1.27° latitude × 2.5° longitude per year) and (b) relative uncertainties (%) in 2020.

3.3 Seasonal pattern of isoprene emissions

Seasonally, the posterior emissions exhibit a pronounced peak during July–September (JAS), and a minimum in December, January, and February (DJF) (Fig. 3). Over the study period (2013–2020), the global mean monthly isoprene emission is approximately 38 TgC month^{-1}, rising by 42% to 54 TgC month^{-1} during JAS and declining sharply by 34% to 25 TgC month^{-1} during DJF. This seasonal cycle differs from that in current bottom-up inventories: MEGAN-MACC (Sindelarova et al., 2014) and MEGAN-ERA5 (also known as CAMS-GLOB-BIOv3.1) (Sindelarova, 2021; Sindelarova et al., 2022), which both display a peak during DJF. This discrepancy primarily stems from an overestimation of isoprene emissions from Oceania (OCE) in current inventories. OCE is estimated to emit up to 92 TgC yr^{-1} in MEGAN-MACC and 52 TgC yr^{-1} in

https://doi.org/10.5194/essd-2025-424
Preprint. Discussion started: 18 August 2025

MEGAN-ERA5—exceeding half of the corresponding emissions from the Amazon (AMZ, 103 and 94 TgC yr^{-1}, respectively)—and exhibits substantial seasonal variability (Fig. S11). Previous studies have attributed this likely overestimation of emissions and its seasonality over OCE to the parameterization of temperature and radiation responses, along with the use of high emission factors in bottom-up models (Emmerson et al., 2016; Emmerson et al., 2018). When OCE is excluded, MEGAN-MACC, and MEGAN-ERA5 inventories show a JAS peak and DJF minimum, which is consistent with our posteriors (Fig. S12). The monthly variability in global isoprene emissions is largely driven by the Northern Hemisphere, mirroring strong seasonal fluctuations in temperature (correlation coefficients, R=0.92) and vegetation activity (R with LAI=0.89) (Figs. 3 and S13; Table S1). While these process relationships are inherently non-linear, correlation analysis provides a useful first-order approximation of regional responses and sensitivities. During JAS, Northern Hemisphere emissions peak at 41 TgC $month^{-1}$ and decline to 10 TgC $month^{-1}$ in DJF, accounting for nearly ~100% of the global JAS–DJF peak-to-trough difference (~30 TgC). In contrast, Southern Hemisphere emissions remain seasonally stable, averaging 14 TgC $month^{-1}$ during both JAS and DJF with negligible difference. This strong hemispheric asymmetry underscores the dominant role of the Northern Hemisphere in shaping the global seasonal cycle. Notably, the synchronicity between monthly emissions and temperature is stronger in the Northern Hemisphere (R=0.96) than in the Southern Hemisphere (R=0.54), further supporting temperature as the primary driver of this pattern. This likely reflects the sharper temperature seasonality in the Northern Hemisphere, whereas oceanic buffering dampens temperature variability in the Southern Hemisphere (Figs. 3b, 3d, and S14). Additionally, LAI seasonality also contributes to the emission cycle, with Northern Hemisphere regions showing stronger LAI variations (Fig. 3e), driven by widespread deciduous and seasonally responsive vegetation (Fig. S15) (Ren et al., 2024; Ma et al., 2023).

https://doi.org/10.5194/essd-2025-424
Preprint. Discussion started: 18 August 2025

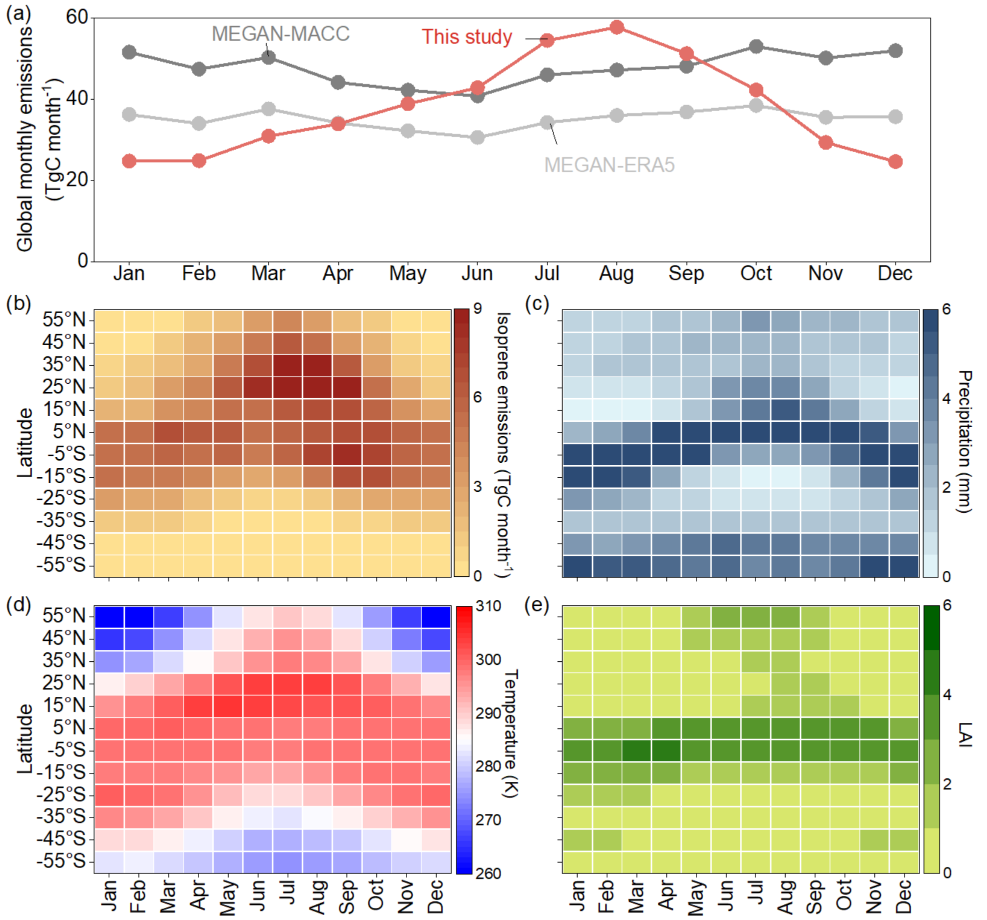

Figure 3. Monthly mean isoprene emissions from 2013 to 2020. (a) shows the global monthly pattern of posterior in this study, MEGAN-MACC (Sindelarova et al., 2014), and MEGAN-ERA5 (also known as CAMS-GLOB-BIOv3.1) inventory (Sindelarova, 2021). MEGAN-ERA5 is based on MEGAN v2.1, updated with ERA5 meteorology and CLM4 land cover (Sindelarova et al., 2022). (b)-(e) display monthly distributions of our estimated isoprene emissions (TgC), precipitation (mm), temperature (K), and the Leaf area index (LAI) by every 10° latitude band, respectively. We here only present the latitude range from 60°S to 60°N where emissions dominate (~99%). Precipitation and temperature are acquired from ERA5; LAI is from Pu et al. (2024). The monthly distributions of two MEGAN inventories are presented in Fig. S16.

3.4 Interannual variation of global isoprene emissions

Over the study period (2013–2020), our global annual isoprene emissions average 456 ± 200 TgC yr^{-1}, falling within the range of existing bottom-up inventories and satellite-based inversion estimates (Fig. 4; Tables S2–S3). This value aligns closely with the MEGAN-ERA5 inventory (422 TgC yr^{-1}), whereas MEGAN-MACC reports a notably higher estimate of 573 TgC yr^{-1}, reflecting a positive bias relative to both our results and other datasets. Such overestimations in earlier MEGAN versions have been documented at global (Bauwens et al., 2016) and regional scales (Kaiser et al., 2018; Gomes Alves et al., 2023).

https://doi.org/10.5194/essd-2025-424
Preprint. Discussion started: 18 August 2025

In terms of interannual variability, global annual isoprene emissions exhibit a standard deviation (1σ) of 14 TgC yr^{-1} over 2013–2020, corresponding to a coefficient of variation of 3.1%. Despite differences in absolute magnitudes, the year-to-year variability simulated by both MEGAN inventories remains broadly consistent with our inversion-based estimates (R=0.62–0.64 for annual emission rates). This temporal coherence underscores the robustness of our posterior in capturing interannual variability. The spatial distribution of interannual variability is highly uneven, with tropical regions such as the AMZ, Equatorial Africa (EQAF), and South Asia (SAS) acting as the principal contributors. These regions show relatively large interannual standard deviations (2–3 TgC yr^{-1}, coefficient of variation: 3.3%-7.6%), primarily due to their status as global isoprene emission hotspots (Fig. 4b). On average, AMZ, EQAF, and SAS account for 15.5%, 11.5%, and 6.7% of global isoprene emissions, with corresponding emission intensities of 10, 6, and 6 gC m^{-2} yr^{-1}, respectively (Fig. 4c).

A positive and a negative anomaly are observed in the interannual variation of global isoprene emissions, associated with the 2019–2020 extreme heat event and post-El Niño cooling in 2017, respectively, highlighting temperature as the primary driver of year-to-year variability. During 2019–2020, annual emissions averaged 478 TgC yr^{-1}, 1.5σ above the 2013–2020 mean (456 TgC yr^{-1}), with 2019 alone reaching 485 TgC yr^{-1} (2σ above the mean) (Fig. S17). This peak coincides with widespread extreme heat (Robinson et al., 2021), with elevated temperatures observed across most regions, except for certain arid and semi-arid tropical zones such as NAF, SAS, and MIDE (Fig. S18). In contrast, emissions dipped to a minimum of 435 TgC yr^{-1} in 2017 (1.5σ below the mean), with a cooling following the extreme 2015–2016 El Niño event, the most intense since 1950 (Hu and Fedorov, 2017). Although partially masked by the subsequent 2019–2020 peak, the 2015–2016 El Niño also triggered an earlier emission enhancement, with global emissions averaging 456 TgC yr^{-1}, exceeding the 2013–2018 baseline mean of 449 TgC yr^{-1} (Fig. S17). During this period, most regions except OCE experienced substantial warming, surpassed only by the more extreme heat of 2019–2020 (Fig. S18). These two identified emission peaks in 2015–2016 and 2019–2020 are consistently reflected in both bottom-up inventories, and satellite observations of HCHO and isoprene concentrations (Fig. S19). Based on these dynamics, we classify the study period into four phases: Phase I: 2013–2014 (average: 447 TgC yr^{-1}); Phase II: 2015–2016 (456 TgC yr^{-1}); Phase III: 2017–2018 (445 TgC yr^{-1}); and Phase IV: 2019–2020 (478 TgC yr^{-1}), to enable clearer analyses and to isolate the distinct emission anomalies associated with major climate events.

https://doi.org/10.5194/essd-2025-424
Preprint. Discussion started: 18 August 2025

Open Access Earth System Science Data Discussions

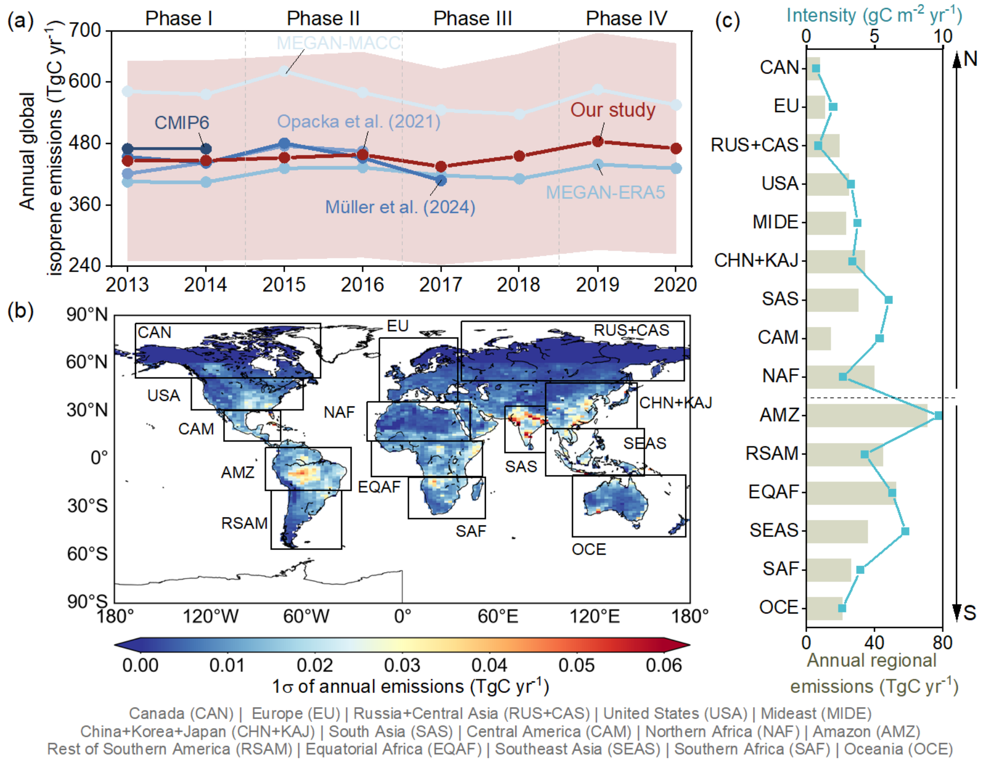

Figure 4. Interannual isoprene emission variations from 2013 to 2020. (a) compares the annual global isoprene emissions among the posterior (red shadow indicate the uncertainty), inventories including MEGAN-MACC, the MEGAN-ERA5 (also known as CAMS-GLOB-BIOv3.1) inventory, ensembles from Opacka et al. (2021), ensembles from CMIP6 (Do et al., 2025), and inversions based on corrected OMI HCHO observations (Müller et al., 2024). (b) plots the global spatial distribution of 1σ of annual isoprene emissions from 2013 to 2020, with frames corresponding to regions discussed in text. (c) depicts the regional annual emissions as well as the emission intensities (defined as the annual isoprene emissions per square meter per year). The regional classification is detailed in Fig. S5 of the SI and full names are listed below the figure.

3.5 Regional contribution to global interannual variations

Tropical regions emerge as the dominant drivers of interannual variability in global isoprene emissions, with the AMZ and RSAM identified as the largest contributors. From Phase I to IV, global emissions exhibit stepwise changes of +2.0%, –2.2%, and +7.2% relative to the preceding phase (Fig. 5a). A regional decomposition of these changes highlights the AMZ and RSAM as the top two contributors. Together, they account for +7 TgC (80.9% of the global increase) during Phase I–II, –9 TgC (89.3% of the global decrease) during Phase II–III, and +9 TgC (27.7% of the global increase) during Phase III–IV. This dominance is attributable to their strong sensitivity to temperature changes, with rough rates of 9.0-25.5 TgC K^{-1} (Figs. 5b-5d). During climate extreme events, including the 2015–2016 El Niño event, subsequent post-El Niño cooling, and the 2019–2020 extreme heat, AMZ and RSAM showed synchronized fluctuations in both temperature and isoprene emissions (Figs. S17–S18). Interestingly, isoprene emissions in these tropical rainforest regions exhibit negative correlations with precipitation and LAI, especially in AMZ (Fig. S20). This suggests that in

https://doi.org/10.5194/essd-2025-424
Preprint. Discussion started: 18 August 2025

the context of persistently high LAI and humidity, temperature acts as the primary regulator, while moderate abiotic stress (e.g., water limitation) may also stimulate isoprene emissions (Loreto and Fineschi, 2015). The spatial distribution further supports this interpretation, with the strongest emission changes concentrated in the core of central Amazon (Fig. 6a). Notably, Phase III–IV shows an amplified sensitivity of isoprene emissions to temperature changes compared to Phase I–II. In Southern America (AMZ+RSAM), response rates increased from 9.6 to 22.7 TgC K^{-1} in AMZ and from 9.0 to 25.0 TgC K^{-1} in RSAM. This suggests that additional factors, such as more widespread increases in radiation during Phase IV (Fig. S21), may have enhanced temperature sensitivity.

However, not all tropical regions exert such impacts on global interannual variations. EQAF and SEAS display limited changes, contributing +1 TgC (7.5%) to the global increase during Phase I–II but offsetting 5.3% of the global decrease in Phase II–III with a net positive change of +1 TgC (Fig. 5a). This muted response reflects regional heterogeneity in climate anomalies and ecosystem characteristics. In EQAF, the 2015-2016 El Niño induced minor changes in temperature and precipitation (Liu et al., 2017), resulting in negligible emission responses (Figs. 5b and 6b). Moreover, EQAF's biome composition—dominated by grasslands (55.4%) and with lower proportions of broadleaf forest (38.9%) compared to AMZ (81.5%)—dampens its emission sensitivity (Fig. S15). In SEAS, widespread peatland fires in 2015 (Field et al., 2016), likely triggered by extremely low precipitation (6.5 mm, 1.5σ below the mean; Fig. S22), may have suppressed biogenic isoprene emissions in Phase II through vegetation loss and ecosystem disturbance (Ciccioli et al., 2014). While emission changes in EQAF and SEAS were negligible during the first three phases, both contributed substantially to the global increase in Phase IV, driven by widespread temperature rises with 1.0σ above their respective means (Figs. 6b and S18).

https://doi.org/10.5194/essd-2025-424
Preprint. Discussion started: 18 August 2025

Open Access Earth System Science Data Discussions

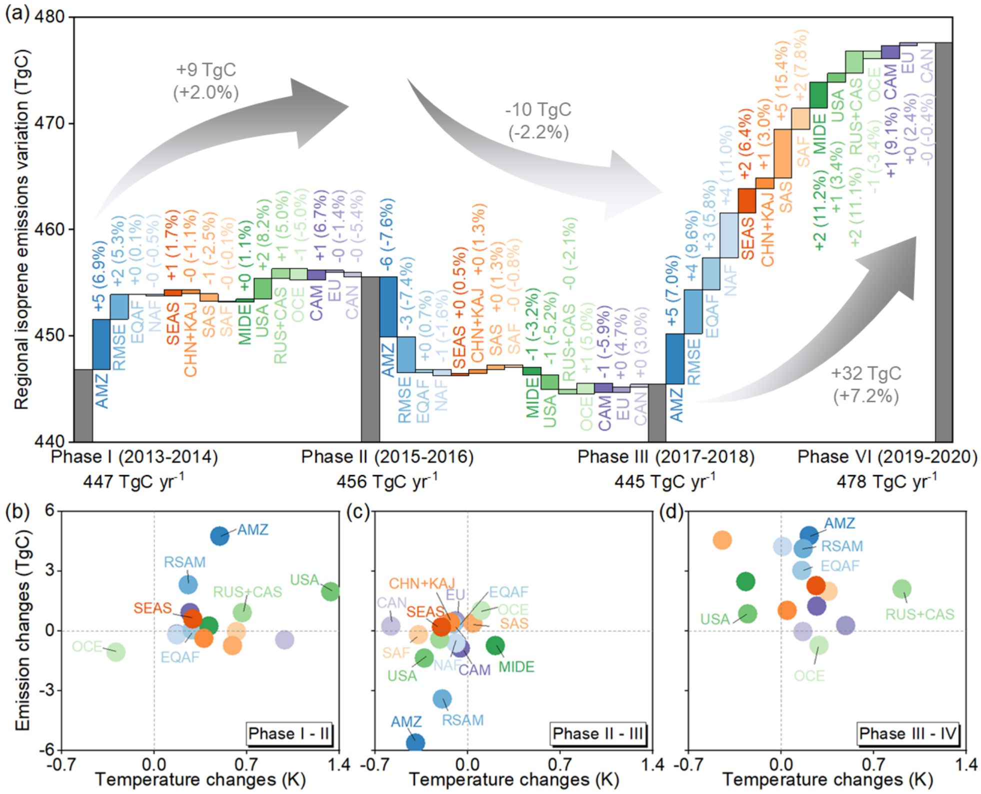

Figure 5. Regional isoprene emission variations and meteorological changes over four phases. (a) presents the regional isoprene emission variation over four phases. (b)-(d) are the scatter plots between changes in regional isoprene emissions and annual temperature from Phase I to II, II to III, and III to IV, respectively. (a)-(d) share the same legend, with colors referring to different regions. Scatter plot of changes in regional isoprene emissions and precipitation, Standardised Precipitation-Evapotranspiration Index (SPEI), LAI, and radiation across phases are presented in Fig. S20.

Occasionally, non-tropical regions also contribute to the global interannual variability, reflecting their sensitivity to extreme climate anomalies. For example, in the USA, emissions increased by 2 TgC (+8.2%) from Phase I to II, making it the third largest contributor to the global increase during this period. In 2016, USA temperatures reached 285.8 K, 1.3σ above its long-term mean (Fig. S18) and the highest warming observed among all regions during the 2015–2016 El Niño. This temperature rise, coupled with enhanced LAI (+0.05) and stable hydrological conditions (Fig. S20), favored increased photosynthetic activity and isoprene biosynthesis, elevating USA’s contribution to Phase II variability.

Conversely, OCE stands out as an exception to the global trend. From Phase I to IV, OCE emissions follow changes of: –1 TgC (–5.0%), +1 TgC (+5.0%), and –1 TgC (–3.4%), which are in opposition to the global variations. This pattern is linked to regional temperature changes (Figs. 5b-5d and S18). OCE was the only region to experience cooling during Phase II (–0.3 K), reaching its lowest temperature of the study period in 2016 (1.1σ below its mean), thereby suppressing emissions. The subsequent temperature rebound (+0.1 K) supported emission recovery from Phase II to III (Figs. 5c and 6c). The Phase IV decline is likely linked to

https://doi.org/10.5194/essd-2025-424
Preprint. Discussion started: 18 August 2025

concurrent reductions in vegetation cover and intensified drought, particularly over northern Australia, where LAI and precipitation decreased by around 0.1-0.2 and 1 mm, respectively (Figs. S23–S25). These factors may have suppressed isoprene emissions despite elevated temperatures.

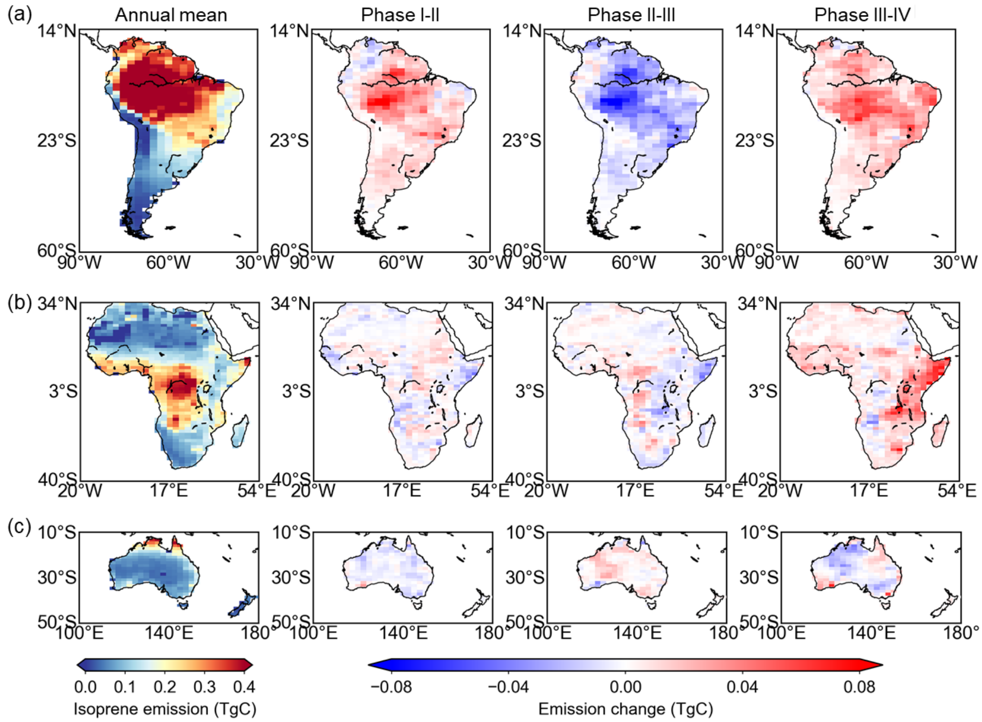

Figure 6. Regional annual mean emissions and their changes across phases for (a) Southern America including AMZ and RSAM, (b) Africa including NAF, EQAF, and SAF, and (c) OCE. The first column shows the annual mean isoprene emissions for each region, and the second to fourth columns correspond to the changes in regional isoprene emission across phases. Corresponding temperature, LAI, and precipitation distributions are shown in Figs. S23, S24 and S25.

3.6 Drivers of regional isoprene emissions on a monthly scale

As discussed above, regional isoprene emissions exhibit strong spatial heterogeneity in their responses to climate anomalies, with temperature generally emerging as the dominant driver. To elucidate the underlying mechanisms and quantify regional sensitivities, we analyzed R between monthly isoprene emissions and key environmental variables—including temperature, precipitation, solar radiation, LAI (Pu et al., 2024), and drought index of Standardised Precipitation-Evapotranspiration Index (SPEI) (ECMWF, 2025)—using both raw monthly values and monthly anomalies (calculated by removing the 2013-2020 mean seasonal cycle for each month) (Figs. 7a–7b). To further assess whether temperature acts independently or interacts with other factors, partial correlation analyses were performed (Figs. 7c–7d). Although biogenic emission processes are inherently non-linear, these correlation analyses provide a useful first-order approximation of regional sensitivities within the dynamic range observed in this study period.

https://doi.org/10.5194/essd-2025-424
Preprint. Discussion started: 18 August 2025

Based on monthly values, isoprene emissions exhibit strong and spatially consistent positive correlations with temperature across most regions (R>0.5, p<0.05; Fig. 7a), except EQAF where no significant correlation is observed. Partial correlation analysis (Fig. 7c) reveals that in many regions, including EU, MIDE, SAS, CAM, NAF, SEAS, and SAF, temperature remains the primary independent driver of emissions, with partial R>0.5 (p<0.05). In contrast, in regions such as CAN, USA, RUS+CAS, CHN+KAJ, AMZ, RSAM, and OCE, the temperature–isoprene relationships weaken or become insignificant after controlling for other factors, suggesting co-regulation by variables such as LAI or radiation. For example, in AMZ, the temperature–isoprene correlation becomes insignificant when controlling for radiation (T|Rad, p>0.05), suggesting radiation as a key co-regulator. This supports earlier findings that AMZ's stronger temperature sensitivity in Phase IV likely reflects interactions with solar radiation. EQAF presents a unique case: although no significant direct correlation with temperature is found, positive partial correlations emerge when controlling for LAI (T|LAI R=0.42) or precipitation (T|P R=0.44), implying that vegetation and moisture dynamics may mask the underlying temperature sensitivity.

When using monthly anomalies to isolate interannual variability, the correlations between temperature anomalies and isoprene anomalies (Fig. 7b) weaken across most regions compared to raw monthly values. This highlights that the strong monthly correlations are largely driven by seasonality rather than interannual coupling. However, in AMZ and OCE, temperature anomalies retain strong positive correlations with isoprene anomalies (R=0.79 and 0.70, respectively), indicating robust interannual temperature sensitivity. Across other regions, temperature anomalies generally remain the dominant driver (R>0, p<0.05), albeit with weaker correlations than in the monthly values. Interestingly, in EQAF, where no direct monthly value correlation exists, temperature anomalies correlate significantly with isoprene anomalies, revealing an interannual sensitivity previously masked by seasonal effects. In regions where temperature anomalies fail to explain interannual variability (e.g., SAS, CAN, RUS+CAS), other drivers emerge. For instance, in SAS, LAI anomalies show the strongest association with isoprene anomalies (R=0.65), underscoring the critical role of vegetation dynamics in controlling its interannual emissions.

Anomaly-based partial correlations further clarify the independent role of temperature anomalies (Fig. 7d). Where direct correlations between temperature anomalies and isoprene anomalies are significant, temperature generally remains an independent driver (partial R>0, p<0.05). Notably, AMZ and OCE sustain strong partial correlations (R>0.5) even after controlling for other variables, confirming their robust temperature sensitivity. In contrast, in regions such as CAN, RUS+CAS, and SAS, where direct temperature–isoprene correlations are insignificant (p>0.05), interannual variability is clearly dominated by other factors. For example, in SAS, LAI anomalies exhibit the strongest (R=0.65 in Fig. 7b) and most independent association with isoprene anomalies, even after controlling for other variables (R=0.49-0.80), underscoring the dominant role of vegetation dynamics in modulating interannual emissions in this region.

https://doi.org/10.5194/essd-2025-424
Preprint. Discussion started: 18 August 2025

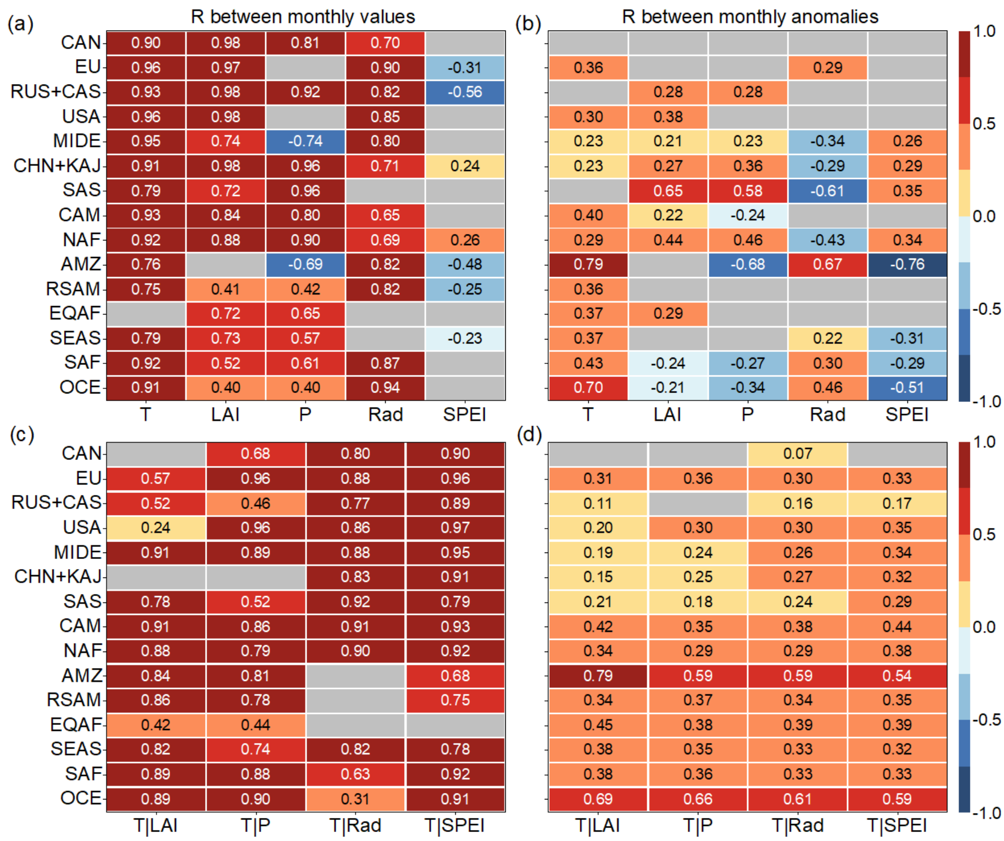

*T=Temperature; LAI=Leaf area index; P=Precipitation; Rad=Radiation; SPEI=Standardized Precipitation-Evapotranspiration Index. (T|xx) indicates partial correlation between Temperature and Emissions after removing the influence of factor xx.

Figure 7. Pearson correlation (R) matrix between regional isoprene emissions and environmental factors on a monthly scale. (a) shows the R matrix between monthly regional isoprene emissions and environmental factors. (c) plots the partial correlation coefficient between temperature and isoprene emissions after removing certain factor's impact. (b) and (d) are plotted for monthly anomalies obtained by removing the mean seasonal cycle as (a) and (c). In all panels, T, P, and Rad represent temperature, precipitation, and radiation, respectively. Regions are ordered from south to north (bottom to top). Gray boxes indicate non-significant correlations (p>0.05).

Overall, within the dynamic range of environmental variables observed during this study period, temperature emerges as the dominant driver of regional isoprene variability, particularly in tropical and temperate regions. This influence is modulated by co-varying factors such as radiation, LAI, and water stress, relative importance varying regionally. The comparison between monthly values and anomalies reveals that much of the apparent temperature dependence at monthly scales reflects seasonality, whereas anomaly-based correlations provide clearer insights into interannual sensitivities and co-regulatory mechanisms. For example, in AMZ, temperature consistently controls emissions and is likely co-regulated by radiation, which may explain the amplified sensitivity observed in Phase IV (Section 3.5). In contrast, in SAS, interannual variability is largely driven by vegetation dynamics, as indicated by strong correlations between isoprene and LAI anomalies even after accounting for other factors.

https://doi.org/10.5194/essd-2025-424
Preprint. Discussion started: 18 August 2025

4. Limitations

While our results demonstrate clear improvements over prior estimates in terms of both spatial distribution and correlation with observations (Figs. 1 and S8-S10), several limitations remain, highlighting areas for future refinement. A primary limitation arises from the incomplete spatial coverage of CrIS observations, particularly at high latitudes (north of 60°N; Fig. S1), where emissions in this study remain unchanged from prior. This omission has limited impact on global totals (~1.0% in prior), as boreal and tundra emissions are minor compared to tropical regions (Guenther et al., 2012). However, warming-driven increases in Arctic isoprene emissions (Seco et al., 2022; Wang et al., 2024d) suggest these regions may become more important in future global budgets and merit closer attention in upcoming inversions. Another limitation stems from comparing CrIS-retrieved isoprene columns with model outputs, as both are subject to uncertainties. The ANN-based retrieval lacks scene-specific vertical sensitivity information, which may bias comparisons in regions with atypical vertical profiles or low information content. Similarly, uncertainties in the LMDZ-INCA model's treatment of isoprene chemistry and transport may propagate into simulated columns. These challenges could be mitigated by future retrievals incorporating vertical sensitivity and by model developments to better represent key isoprene processes.

Beyond satellite-related issues, several methodological constraints inherent to the inversion framework must be acknowledged. The FDMB approach assumes a localized linear relationship between surface emissions and atmospheric column concentrations, which simplifies the complex, non-linear chemistry of isoprene. This assumption is partly justified because CrIS observations are acquired near 13:30 local time, when OH concentrations peak and isoprene lifetimes are shortest (Hard et al., 1986; Karl et al., 2004). Moreover, this linearization is supported by sensitivity tests with varying perturbation magnitudes and improved posterior fits to CrIS observations. Nevertheless, in high-isoprene, low-NO_x regions like the Amazon, where OH levels are limited (Zhao et al., 2025; Yoon, 2025), this linearity may break down. Future work could adopt joint NO_x–isoprene inversions or iterative schemes (Wells et al., 2020), to better capture the strong chemical coupling between NO_x, OH, and isoprene.

5. Data and code availability

All the data and model code are openly available. The isoprene emission data in this study are deposited in Zenodo (https://doi.org/10.5281/zenodo.16214776) (Hui et al., 2025). Other data include: the OMPS HCHO products are available in the NASA GES DISC for OMPS/Suomi-NPP (https://doi.org/10.5067/IIM1GHT07QA8); the TROPOMI HCHO products are available at https://sentiwiki.copernicus.eu/web/s5p-products; the 2013–2020 climatological means of the CrIS isoprene columns are available at https://doi.org/10.13020/5n0j-wx73 (Wells et al., 2022). All the meteorological factors (temperature, precipitation, and radiation) are acquired from ERA5 dataset at https://cds.climate.copernicus.eu/datasets/reanalysis-era5-land-monthly-means?tab=overview. Land cover data from 2013 to 2020 are ESA Land Cover Climate Change Initiative (Land_Cover_cci): Global Plant

https://doi.org/10.5194/essd-2025-424
Preprint. Discussion started: 18 August 2025

Functional Types (PFT) Dataset, v2.0.8, acquired from https://catalogue.ceda.ac.uk/uuid/26a0f46c95ee4c29b5c650b129aab788/. Pandonia Global Network (PGN) surface observed HCHO area acquired from https://www.pandonia-global-network.org/. The drought indices, i.e., the Standardised Precipitation-Evapotranspiration Index (SPEI), are obtained from ECMWF (https://xds-preprod.ecmwf.int/datasets/derived-drought-historical-monthly?tab=overview). Leaf area index (LAI) data are acquired from Pu et al. (2024). The codes and scripts developed for inversions, plotting, and other analysis are accessible upon reasonable request from the corresponding author. The version of the LMDZ-INCA model used in this study is available from: https://forge.ipsl.jussieu.fr/igcmg/svn/modipsl/trunk.

6. Implication

This study provides, to our knowledge, the first global, multi-year (2013–2020) estimates of isoprene emissions derived directly from satellite-retrieved isoprene concentrations, offering valuable insights into the temporal and spatial drivers of emission variability. Our analysis reveals the dominant influence of climate anomalies in shaping both global and regional variability. On interannual timescales, two major emission peaks in 2015–2016 and 2019–2020 coincide with El Niño and widespread extreme heat events, driven primarily by temperature-induced enhancements in tropical regions, especially the Amazon. Seasonally, global emissions peak during July–September and reach a minimum in December–February, reflecting the pronounced seasonality of temperature and vegetation activity in the Northern Hemisphere. These findings underscore the high sensitivity of biogenic emissions to climatic variability across timescales, particularly in regions with dense vegetation and strong meteorological forcing. Given the sub-decadal scope of this study, the analysis has focused on short-term climate variability—especially temperature—as the principal driver, while long-term influences such as land cover change and rising atmospheric CO_2 concentrations are not explicitly addressed. Extending this framework to multi-decadal periods will be essential to disentangle the interplay between short- and long-term drivers and to assess their combined impacts on atmospheric chemistry and climate feedbacks.

In the context of this eight-year study, the occurrence of two major climate anomalies—El Niño and widespread extreme heat events—supports the focus on extreme weather, which exerts disproportionate impacts on isoprene emissions. Looking ahead, however, the convergence of multiple environmental stressors, including global warming (Armstrong Mckay et al., 2022), deforestation in tropical regions (Leite-Filho et al., 2021), rising atmospheric CO_2 (with its dual fertilization and inhibition effects) (Cheng et al., 2022; Sahu et al., 2023), and the increasing frequency and intensity of climate extremes (wildfires, floods, and droughts) (Newman and Noy, 2023; Gebrechorkos et al., 2025; Zheng et al., 2023), raise critical questions about the long-term trajectory of global isoprene emissions. A key uncertainty is whether these interacting pressures will collectively amplify or suppress future emissions. Given isoprene's central role in regulating atmospheric oxidative capacity, such dynamics profoundly influence broader climate feedbacks. For instance, a sustained decline in isoprene emissions may elevate OH radical concentrations, thereby accelerating the atmospheric removal of CH_4 and other species (Zhao et al., 2025). However, the magnitude and direction of such feedbacks remain poorly constrained, highlighting the need for continued advancements in satellite observations and modeling tools to better characterize isoprene emissions and their interactions within the coupled biosphere–atmosphere system under future climate scenarios.

Acknowledgements

This work was supported by the National Key R&D Program of China (Grant Nos. 2023YFC3709202), was granted access to the HPC resources of TGCC under the allocation A0170102201 made by GENCI, and was funded by ESA WORld EMission (WOREM) project (https://www.world-emission.com). We wish to thank J. Bruna (LSCE) and his team for computer support and the use of the OBELIX computing facility at LSCE. DBM and KCW acknowledge support from NASA GMAO (grant #80NSSC23K0520).

Author contributions

HL designed this study, conducted the emission inversions, analyzed the data, and wrote the draft. PC, DH, BZ, and GB supervised the study, helped data analysis, reviewed and edited the paper. PK performed the LMDZ-INCA simulations, helped data analysis, and edited the paper. DB and KW offered the CrIS isoprene data, reviewed and edited the paper. FC and JL reviewed and edited the paper. All the co-authors contributed to the revision of this paper.

Competing interests

At least one of the (co-)authors is a member of the editorial board of *Earth System Science Data*. The authors have no other competing interests to declare.

Reference

Abad, G. G.: OMPS-NPP L2 NM Formaldehyde (HCHO) Total Column swath orbital V1, Greenbelt, MD, USA, Goddard Earth Sciences Data and Information Services Center (GES DISC), 10.5067/IIM1GHT07QA8, 2022.

Armstrong McKay, D. I., Staal, A., Abrams, J. F., Winkelmann, R., Sakschewski, B., Loriani, S., Fetzer, I., Cornell, S. E., Rockström, J., and Lenton, T. M.: Exceeding 1.5°C global warming could trigger multiple climate tipping points, Science, 377, eabn7950, doi:10.1126/science.abn7950, 2022.

Barkley, M. P., Smedt, I. D., Van Roozendael, M., Kurosu, T. P., Chance, K., Arneth, A., Hagberg, D., Guenther, A., Paulot, F., Marais, E., et al.: Top-down isoprene emissions over tropical South America inferred from SCIAMACHY and OMI formaldehyde columns, Journal of Geophysical Research: Atmospheres, 118, 6849-6868, https://doi.org/10.1002/jgrd.50552, 2013.

Bates, K. H. and Jacob, D. J.: A new model mechanism for atmospheric oxidation of isoprene: global effects on oxidants, nitrogen oxides, organic products, and secondary organic aerosol, Atmos. Chem. Phys., 19, 9613-9640, 10.5194/acp-19-9613-2019, 2019.

Bauwens, M., Stavrakou, T., Müller, J. F., De Smedt, I., Van Roozendael, M., van der Werf, G. R., Wiedinmyer, C., Kaiser, J. W., Sindelarova, K., and Guenther, A.: Nine years of global hydrocarbon emissions based on source inversion of OMI formaldehyde observations, Atmos. Chem. Phys., 16, 10133-10158, 10.5194/acp-16-10133-2016, 2016.

Cao, Y., Yue, X., Lei, Y., Zhou, H., Liao, H., Song, Y., Bai, J., Yang, Y., Chen, L., Zhu, J., et al.: Identifying the Drivers of Modeling Uncertainties in Isoprene Emissions: Schemes Versus Meteorological Forcings, Journal of Geophysical Research: Atmospheres, 126, e2020JD034242, https://doi.org/10.1029/2020JD034242, 2021.

Cheng, W., Dan, L., Deng, X., Feng, J., Wang, Y., Peng, J., Tian, J., Qi, W., Liu, Z., Zheng, X., et al.: Global monthly gridded atmospheric carbon dioxide concentrations under the historical and future scenarios, Scientific Data, 9, 83, 10.1038/s41597-022-01196-7, 2022.

Choi, J., Henze, D. K., Wells, K. C., and Millet, D. B.: Joint Inversion of Satellite-Based Isoprene and Formaldehyde Observations to Constrain Emissions of Nonmethane Volatile Organic Compounds, Journal of Geophysical Research: Atmospheres, 130, e2024JD042070, https://doi.org/10.1029/2024JD042070, 2025.

Ciccioli, P., Centritto, M., and Loreto, F.: Biogenic volatile organic compound emissions from vegetation fires, Plant, Cell & Environment, 37, 1810-1825, https://doi.org/10.1111/pce.12336, 2014.

Cooper, M., Martin, R. V., Padmanabhan, A., and Henze, D. K.: Comparing mass balance and adjoint methods for inverse modeling of nitrogen dioxide columns for global nitrogen oxide emissions, Journal of Geophysical Research: Atmospheres, 122, 4718-4734, https://doi.org/10.1002/2016JD025985, 2017.

Curtius, J., Heinritzi, M., Beck, L. J., Pöhlker, M. L., Tripathi, N., Krumm, B. E., Holzbeck, P., Nussbaumer, C. M., Hernández Pardo, L., Klimach, T., et al.: Isoprene nitrates drive new particle formation in Amazon's upper troposphere, Nature, 636, 124-130, 10.1038/s41586-024-08192-4, 2024.

Do, N. T. N., Sudo, K., Ito, A., Emmons, L. K., Naik, V., Tsigaridis, K., Seland, Ø., Folberth, G. A., and Kelley, D. I.: Historical trends and controlling factors of isoprene emissions in CMIP6 Earth system models, Geosci. Model Dev., 18, 2079-2109, 10.5194/gmd-18-2079-2025, 2025.

ECMWF: Monthly drought indices from 1940 to present derived from ERA5 reanalysis. ECMWF Cross Data Store (ECDS). 10.24381/9bea5e16 (Accessed on 06-06-2025), 2025.

Emmerson, K. M., Cope, M. E., Galbally, I. E., Lee, S., and Nelson, P. F.: Isoprene and monoterpene emissions in south-east Australia: comparison of a multi-layer canopy model with MEGAN and with atmospheric observations, Atmos. Chem. Phys., 18, 7539-7556, 10.5194/acp-18-7539-2018, 2018.

Emmerson, K. M., Galbally, I. E., Guenther, A. B., Paton-Walsh, C., Guerette, E. A., Cope, M. E., Keywood, M. D., Lawson, S. J., Molloy, S. B., Dunne, E., et al.: Current estimates of biogenic emissions from eucalypts uncertain for southeast Australia, Atmos. Chem. Phys., 16, 6997-7011, 10.5194/acp-16-6997-2016, 2016.

ESA: S5P_L2__HCHO___HiR. Version 2. Sentinel-5P TROPOMI Tropospheric Formaldehyde HCHO 1-Orbit L2 5.5km x 3.5km. Greenbelt, MD, USA. Archived by National Aeronautics and Space Administration, U.S. Government, Goddard Earth Sciences Data and Information Services Center (GES DISC). 10.5270/S5P-vg1i7t0, 2020.

Field, R. D., van der Werf, G. R., Fanin, T., Fetzer, E. J., Fuller, R., Jethva, H., Levy, R., Livesey, N. J., Luo, M., Torres, O., et al.: Indonesian fire activity and smoke pollution in 2015 show persistent nonlinear sensitivity to El Niño-induced drought, Proceedings of the National Academy of Sciences, 113, 9204-9209, doi:10.1073/pnas.1524888113, 2016.

https://doi.org/10.5194/essd-2025-424
Preprint. Discussion started: 18 August 2025

Fu, D., Millet, D. B., Wells, K. C., Payne, V. H., Yu, S., Guenther, A., and Eldering, A.: Direct retrieval of isoprene from satellite-based infrared measurements, Nature Communications, 10, 3811, 10.1038/s41467-019-11835-0, 2019.

Gebrechorkos, S. H., Sheffield, J., Vicente-Serrano, S. M., Funk, C., Miralles, D. G., Peng, J., Dyer, E., Talib, J., Beck, H. E., Singer, M. B., et al.: Warming accelerates global drought severity, Nature, 10.1038/s41586-025-09047-2, 2025.

Geddes, J. A., Pusede, S. E., and Wong, A. Y. H.: Changes in the Relative Importance of Biogenic Isoprene and Soil NO_x Emissions on Ozone Concentrations in Nonattainment Areas of the United States, Journal of Geophysical Research: Atmospheres, 127, e2021JD036361, https://doi.org/10.1029/2021JD036361, 2022.

Gomes Alves, E., Aquino Santana, R., Quaresma Dias-Júnior, C., Botía, S., Taylor, T., Yáñez-Serrano, A. M., Kesselmeier, J., Bourtsoukidis, E., Williams, J., Lembo Silveira de Assis, P. I., et al.: Intra- and interannual changes in isoprene emission from central Amazonia, Atmos. Chem. Phys., 23, 8149-8168, 10.5194/acp-23-8149-2023, 2023.

Guenther, A. B., Jiang, X., Heald, C. L., Sakulyanontvittaya, T., Duhl, T., Emmons, L. K., and Wang, X.: The Model of Emissions of Gases and Aerosols from Nature version 2.1 (MEGAN2.1): an extended and updated framework for modeling biogenic emissions, Geosci. Model Dev., 5, 1471-1492, 10.5194/gmd-5-1471-2012, 2012.

Hard, T. M., Chan, C. Y., Mehrabzadeh, A. A., Pan, W. H., and O'Brien, R. J.: Diurnal cycle of tropospheric OH, Nature, 322, 617-620, 10.1038/322617a0, 1986.

Hauglustaine, D. A., Hourdin, F., Jourdain, L., Filiberti, M. A., Walters, S., Lamarque, J. F., and Holland, E. A.: Interactive chemistry in the Laboratoire de Météorologie Dynamique general circulation model: Description and background tropospheric chemistry evaluation, Journal of Geophysical Research: Atmospheres, 109, https://doi.org/10.1029/2003JD003957, 2004.

Henrot, A. J., Stanelle, T., Schröder, S., Siegenthaler, C., Taraborrelli, D., and Schultz, M. G.: Implementation of the MEGAN (v2.1) biogenic emission model in the ECHAM6-HAMMOZ chemistry climate model, Geosci. Model Dev., 10, 903-926, 10.5194/gmd-10-903-2017, 2017.

Hu, S. and Fedorov, A. V.: The extreme El Niño of 2015–2016 and the end of global warming hiatus, Geophysical Research Letters, 44, 3816-3824, https://doi.org/10.1002/2017GL072908, 2017.

Hui, L., Philippe, C., Pramod, K., Didier A., H., Frédéric, C., Grégoire, B., Dylan B., M., Kelley C., W., Jinghui, L., and Bo, Z.: Global biogenic isoprene emissions 2013-2020 inferred from satellite isoprene observations, Zenodo., https://doi.org/10.5281/zenodo.16214776, 2025.

Kaiser, J., Jacob, D. J., Zhu, L., Travis, K. R., Fisher, J. A., González Abad, G., Zhang, L., Zhang, X., Fried, A., Crounse, J. D., et al.: High-resolution inversion of OMI formaldehyde columns to quantify isoprene emission on ecosystem-relevant scales: application to the southeast US, Atmos. Chem. Phys., 18, 5483-5497, 10.5194/acp-18-5483-2018, 2018.

Karl, M., Brauers, T., Dorn, H. P., Holland, F., Komenda, M., Poppe, D., Rohrer, F., Rupp, L., Schaub, A., and Wahner, A.: Kinetic Study of the OH-isoprene and O_3-isoprene reaction in the atmosphere simulation chamber, SAPHIR, Geophysical Research Letters, 31, https://doi.org/10.1029/2003GL019189, 2004.

Kumar, P., Broquet, G., Hauglustaine, D., Beaudor, M., Clarisse, L., Van Damme, M., Coheur, P., Cozic, A., Zheng, B., Revilla Romero, B., et al.: Global atmospheric inversion of the NH_3 emissions over 2019-2022 using the LMDZ-INCA chemistry-transport model and the IASI NH_3 observations, EGUsphere, 2025, 1-32, 10.5194/egusphere-2025-162, 2025.

Leite-Filho, A. T., Soares-Filho, B. S., Davis, J. L., Abrahão, G. M., and Börner, J.: Deforestation reduces rainfall and agricultural revenues in the Brazilian Amazon, Nature Communications, 12, 2591, 10.1038/s41467-021-22840-7, 2021.

Liu, J., Bowman, K. W., Schimel, D. S., Parazoo, N. C., Jiang, Z., Lee, M., Bloom, A. A., Wunch, D., Frankenberg, C., Sun, Y., et al.: Contrasting carbon cycle responses of the tropical continents to the 2015–2016 El Niño, Science, 358, eaam5690, doi:10.1126/science.aam5690, 2017.

Loreto, F. and Fineschi, S.: Reconciling functions and evolution of isoprene emission in higher plants, New Phytologist, 206, 578-582, https://doi.org/10.1111/nph.13242, 2015.

Ma, H., Crowther, T. W., Mo, L., Maynard, D. S., Renner, S. S., van den Hoogen, J., Zou, Y., Liang, J., de-Miguel, S., Nabuurs, G.-J., et al.: The global biogeography of tree leaf form and habit, Nature Plants, 9, 1795-1809, 10.1038/s41477-023-01543-5, 2023.

Marais, E. A., Jacob, D. J., Kurosu, T. P., Chance, K., Murphy, J. G., Reeves, C., Mills, G., Casadio, S., Millet, D. B., Barkley, M. P., et al.: Isoprene emissions in Africa inferred from OMI observations of formaldehyde columns, Atmos. Chem. Phys., 12, 6219-6235, 10.5194/acp-12-6219-2012, 2012.

McDuffie, E. E., Smith, S. J., O'Rourke, P., Tibrewal, K., Venkataraman, C., Marais, E. A., Zheng, B., Crippa, M., Brauer, M., and Martin, R. V.: A global anthropogenic emission inventory of atmospheric pollutants from sector- and fuel-specific sources (1970–2017): an application of the Community Emissions Data System (CEDS), Earth Syst. Sci. Data, 12, 3413-3442, 10.5194/essd-12-3413-2020, 2020.

Messina, P., Lathière, J., Sindelarova, K., Vuichard, N., Granier, C., Ghattas, J., Cozic, A., and Hauglustaine, D. A.: Global biogenic volatile organic compound emissions in the ORCHIDEE and MEGAN models and sensitivity to key parameters, Atmos. Chem. Phys., 16, 14169-14202, 10.5194/acp-16-14169-2016, 2016.

Millet, D. B., Jacob, D. J., Boersma, K. F., Fu, T.-M., Kurosu, T. P., Chance, K., Heald, C. L., and Guenther, A.: Spatial distribution of isoprene emissions from North America derived from formaldehyde column measurements by the OMI satellite sensor, Journal of Geophysical Research: Atmospheres, 113, https://doi.org/10.1029/2007JD008950, 2008.

Müller, J. F., Stavrakou, T., Oomen, G. M., Opacka, B., De Smedt, I., Guenther, A., Vigouroux, C., Langerock, B., Aquino, C. A. B., Grutter, M., et al.: Bias correction of OMI HCHO columns based on FTIR and aircraft measurements and impact on top-down emission estimates, Atmos. Chem. Phys., 24, 2207-2237, 10.5194/acp-24-2207-2024, 2024.

Newman, R. and Noy, I.: The global costs of extreme weather that are attributable to climate change, Nature Communications, 14, 6103, 10.1038/s41467-023-41888-1, 2023.

Nowlan, C. R., González Abad, G., Kwon, H.-A., Ayazpour, Z., Chan Miller, C., Chance, K., Chong, H., Liu, X., O'Sullivan, E., Wang, H., et al.: Global Formaldehyde Products From the Ozone Mapping and Profiler Suite (OMPS) Nadir Mappers on Suomi NPP and NOAA-20, Earth and Space Science, 10, e2022EA002643, https://doi.org/10.1029/2022EA002643, 2023.

Nussbaumer, C. M., Crowley, J. N., Schuladen, J., Williams, J., Hafermann, S., Reiffs, A., Axinte, R., Harder, H., Ernest, C., Novelli, A., et al.: Measurement report: Photochemical production and loss rates of formaldehyde and ozone across Europe, Atmos. Chem. Phys., 21, 18413-18432, 10.5194/acp-21-18413-2021, 2021.

Opacka, B., Müller, J. F., Stavrakou, T., Bauwens, M., Sindelarova, K., Markova, J., and Guenther, A. B.: Global and regional impacts of land cover changes on isoprene emissions derived from spaceborne data and the MEGAN model, Atmos. Chem. Phys., 21, 8413-8436, 10.5194/acp-21-8413-2021, 2021.

Pacifico, F., Folberth, G. A., Jones, C. D., Harrison, S. P., and Collins, W. J.: Sensitivity of biogenic isoprene emissions to past, present, and future environmental conditions and implications for atmospheric chemistry, Journal of Geophysical Research: Atmospheres, 117, https://doi.org/10.1029/2012JD018276, 2012.

Palmer, P. I., Marvin, M. R., Siddans, R., Kerridge, B. J., and Moore, D. P.: Nocturnal survival of isoprene linked to formation of upper tropospheric organic aerosol, Science, 375, 562-566, 10.1126/science.abg4506, 2022.

Pound, R. J., Durcan, D. P., Evans, M. J., and Carpenter, L. J.: Comparing the Importance of Iodine and Isoprene on Tropospheric Photochemistry, Geophysical Research Letters, 50, e2022GL100997, https://doi.org/10.1029/2022GL100997, 2023.

Pu, J., Yan, K., Roy, S., Zhu, Z., Rautiainen, M., Knyazikhin, Y., and Myneni, R. B.: Sensor-independent LAI/FPAR CDR: reconstructing a global sensor-independent climate data record of MODIS and VIIRS LAI/FPAR from 2000 to 2022, Earth Syst. Sci. Data, 16, 15-34, 10.5194/essd-16-15-2024, 2024.

Ren, Y., Qiu, J., Zeng, Z., Liu, X., Sitch, S., Pilegaard, K., Yang, T., Wang, S., Yuan, W., and Jain, A. K.: Earlier spring greening in Northern Hemisphere terrestrial biomes enhanced net ecosystem productivity in summer, Communications Earth & Environment, 5, 122, 10.1038/s43247-024-01270-5, 2024.

Robinson, A., Lehmann, J., Barriopedro, D., Rahmstorf, S., and Coumou, D.: Increasing heat and rainfall extremes now far outside the historical climate, npj Climate and Atmospheric Science, 4, 45, 10.1038/s41612-021-00202-w, 2021.

Sahu, A., Mostofa, M. G., Weraduwage, S. M., and Sharkey, T. D.: Hydroxymethylbutenyl diphosphate accumulation reveals MEP pathway regulation for high CO_2-induced suppression of isoprene emission, Proceedings of the National Academy of Sciences, 120, e2309536120, doi:10.1073/pnas.2309536120, 2023.

Seco, R., Holst, T., Davie-Martin, C. L., Simin, T., Guenther, A., Pirk, N., Rinne, J., and Rinnan, R.: Strong isoprene emission response to temperature in tundra vegetation, Proceedings of the National Academy of Sciences, 119, e2118014119, doi:10.1073/pnas.2118014119, 2022.

Sindelarova, K., Markova, J., Simpson, D., Huszar, P., Karlicky, J., Darras, S., and Granier, C.: High-resolution biogenic global emission inventory for the time period 2000–2019 for air quality modelling, Earth Syst. Sci. Data, 14, 251-270, 10.5194/essd-14-251-2022, 2022.

https://doi.org/10.5194/essd-2025-424
Preprint. Discussion started: 18 August 2025

Sindelarova, K., Granier, C., Bouarar, I., Guenther, A., Tilmes, S., Stavrakou, T., Müller, J. F., Kuhn, U., Stefani, P., and Knorr, W.: Global data set of biogenic VOC emissions calculated by the MEGAN model over the last 30 years, Atmos. Chem. Phys., 14, 9317-9341, 10.5194/acp-14-9317-2014, 2014.

Sindelarova, K., Markova, J., Simpson, D., Huszar, P., Karlicky, J.,Darras, S., and Granier, C: Copernicus Atmosphere Monitoring Service Global Biogenic VOC emissions version 3.1 (CAMSGLOB-BIOv3.1), Copernicus Atmosphere Monitoring Service, ECCAD, https://doi.org/10.24380/cv4p-5f79, 2021.

Sun, S., Palmer, P. I., Siddans, R., Kerridge, B. J., Ventress, L., Edtbauer, A., Ringsdorf, A., Pfannerstill, E. Y., and Williams, J.: Seasonal isoprene emission estimates over tropical South America inferred from satellite observations of isoprene, EGUsphere, 2025, 1-28, 10.5194/egusphere-2025-778, 2025.

Unger, N.: Isoprene emission variability through the twentieth century, Journal of Geophysical Research: Atmospheres, 118, 13,606-613,613, https://doi.org/10.1002/2013JD020978, 2013.

Valin, L. C., Fiore, A. M., Chance, K., and González Abad, G.: The role of OH production in interpreting the variability of CH_2O columns in the southeast U.S, Journal of Geophysical Research: Atmospheres, 121, 478-493, https://doi.org/10.1002/2015JD024012, 2016.

van der Werf, G. R., Randerson, J. T., Giglio, L., van Leeuwen, T. T., Chen, Y., Rogers, B. M., Mu, M., van Marle, M. J. E., Morton, D. C., Collatz, G. J., et al.: Global fire emissions estimates during 1997–2016, Earth Syst. Sci. Data, 9, 697-720, 10.5194/essd-9-697-2017, 2017.

Wang, H., Liu, X., Wu, C., and Lin, G.: Regional to global distributions, trends, and drivers of biogenic volatile organic compound emission from 2001 to 2020, Atmos. Chem. Phys., 24, 3309-3328, 10.5194/acp-24-3309-2024, 2024a.

Wang, H., Nagalingam, S., Welch, A. M., Leong, C., Czimczik, C. I., and Guenther, A. B.: Heat waves may trigger unexpected surge in aerosol and ozone precursor emissions from sedges in urban landscapes, Proceedings of the National Academy of Sciences, 121, e2412817121, doi:10.1073/pnas.2412817121, 2024b.

Wang, H., Welch, A., Nagalingam, S., Leong, C., Kittitananuvong, P., Barsanti, K. C., Sheesley, R. J., Czimczik, C. I., and Guenther, A. B.: Arctic Heatwaves Could Significantly Influence the Isoprene Emissions From Shrubs, Geophysical Research Letters, 51, e2023GL107599, https://doi.org/10.1029/2023GL107599, 2024c.

Wang, H., Welch, A. M., Nagalingam, S., Leong, C., Czimczik, C. I., Tang, J., Seco, R., Rinnan, R., Vettikkat, L., Schobesberger, S., et al.: High temperature sensitivity of Arctic isoprene emissions explained by sedges, Nature Communications, 15, 6144, 10.1038/s41467-024-49960-0, 2024d.

Weber, J., King, J. A., Sindelarova, K., and Val Martin, M.: Updated isoprene and terpene emission factors for the Interactive BVOC (iBVOC) emission scheme in the United Kingdom Earth System Model (UKESM1.0), Geosci. Model Dev., 16, 3083-3101, 10.5194/gmd-16-3083-2023, 2023.

Wells, K. C., Millet, D. B., Payne, V. H., Deventer, M. J., Bates, K. H., de Gouw, J. A., Graus, M., Warneke, C., Wisthaler, A., and Fuentes, J. D.: Satellite isoprene retrievals constrain emissions and atmospheric oxidation, Nature, 585, 225-233, 10.1038/s41586-020-2664-3, 2020.

Wells, K. C., Millet, D. B., Payne, V. H., Vigouroux, C., Aquino, C. A. B., De Mazière, M., de Gouw, J. A., Graus, M., Kurosu, T., Warneke, C., et al.: Next-Generation Isoprene Measurements From Space: Detecting Daily Variability at High Resolution, Journal of Geophysical Research: Atmospheres, 127, e2021JD036181, https://doi.org/10.1029/2021JD036181, 2022.

Wennberg, P. O., Bates, K. H., Crounse, J. D., Dodson, L. G., McVay, R. C., Mertens, L. A., Nguyen, T. B., Praske, E., Schwantes, R. H., Smarte, M. D., et al.: Gas-Phase Reactions of Isoprene and Its Major Oxidation Products, Chemical Reviews, 118, 3337-3390, 10.1021/acs.chemrev.7b00439, 2018.

Wolfe, G. M., Kaiser, J., Hanisco, T. F., Keutsch, F. N., de Gouw, J. A., Gilman, J. B., Graus, M., Hatch, C. D., Holloway, J., Horowitz, L. W., et al.: Formaldehyde production from isoprene oxidation across NO_x regimes, Atmos. Chem. Phys., 16, 2597-2610, 10.5194/acp-16-2597-2016, 2016.

Xu, Z. N., Nie, W., Liu, Y. L., Sun, P., Huang, D. D., Yan, C., Krechmer, J., Ye, P. L., Xu, Z., Qi, X. M., et al.: Multifunctional Products of Isoprene Oxidation in Polluted Atmosphere and Their Contribution to SOA, Geophysical Research Letters, 48, e2020GL089276, https://doi.org/10.1029/2020GL089276, 2021.

Yoon, J. Y. S., Wells, K. C., Millet, D. B., Swann, A. S., Thornton, J. A., Turner, A. J.: Impacts of interannual isoprene variations on methane lifetimes and trends, Geophysical Research Letters, in press, 2025.

Zhao, Y., Zheng, B., Saunois, M., Ciais, P., Hegglin, M. I., Lu, S., Li, Y., and Bousquet, P.: Air pollution modulates trends and variability of the global methane budget, Nature, 10.1038/s41586-025-09004-z, 2025.

Zheng, B., Ciais, P., Chevallier, F., Yang, H., Canadell, J. G., Chen, Y., van der Velde, I. R., Aben, I., Chuvieco, E., Davis, S. J., et al.: Record-high CO_2 emissions from boreal fires in 2021, Science, 379, 912-917, doi:10.1126/science.ade0805, 2023.